PNAS RESEARCH ARTICLE | APPLIED PHYSICAL SCIENCES

Nanoscale chemical imaging with structured X-ray illumination

Jizhou Li[a,b,1], Si Chen[c], Daniel Ratner[d], Thierry Blu[e], Piero Pianetta[a], and Yijin Liu[f,1]

Edited by David Weitz, Harvard University, Cambridge, MA; received August 23, 2023; accepted October 23, 2023

High-resolution imaging with compositional and chemical sensitivity is crucial for a wide range of scientific and engineering disciplines. Although synchrotron X-ray imaging through spectromicroscopy has been tremendously successful and broadly applied, it encounters challenges in achieving enhanced detection sensitivity, satisfactory spatial resolution, and high experimental throughput simultaneously. In this work, based on structured illumination, we develop a single-pixel X-ray imaging approach coupled with a generative image reconstruction model for mapping the compositional heterogeneity with nanoscale resolvability. This method integrates a full-field transmission X-ray microscope with an X-ray fluorescence detector and eliminates the need for nanoscale X-ray focusing and raster scanning. We experimentally demonstrate the effectiveness of our approach by imaging a battery sample composed of mixed cathode materials and successfully retrieving the compositional variations of the imaged cathode particles. Bridging the gap between structural and chemical characterizations using X-rays, this technique opens up vast opportunities in the fields of biology, environmental, and materials science, especially for radiation-sensitive samples.

X ray chemical imaging | transmission X ray microscopy | image reconstruction | X ray fluorescence | synchrotron X rays

Significance

High-resolution imaging that can reveal chemical details is vital across numerous scientific fields. However, current methods struggle to balance resolution, sensitivity, and speed. The proposed NxSCI approach utilizes structured illumination to create a unique X-ray chemical imaging technique. It allows for detailed mapping at a nanoscale without needing highly focused X-rays or slow scanning processes. By applying this to a battery sample, we showcased its potential to unveil intricate compositional differences. This technique has broad implications, offering advanced imaging solutions in biology, environmental studies, and materials science, and is especially beneficial for samples sensitive to radiation.

Imaging at fine spatial resolution with high compositional and chemical sensitivity is highly desirable in various scientific and engineering applications (1–5). For example, metal contamination in Si wafers, in the forms of particles, molecules and/or atoms, can jeopardize the manufacturing of integrated circuits and, thus, exhibit very significant impacts in the semiconductor industry (6). Under aggressive battery operation in lithium-ion batteries, the cathode material dissolves and precipitates onto the anode with a random and sparse distribution, causing performance degradation and potential safety concerns (4, 7, 8). Generally speaking, the compositional heterogeneities, from the material level to the device level, either purposely engineered or unintentionally formed, have important implications in many high-profile research areas, including electrochemical energy conversion and storage, critical materials mining and upcycling, environmental remediation, biomedical applications, etc. Therefore, visualizing the spatial distribution of elements of interest and understanding their dynamic behavior are important to both fundamental research and practical applications.

X-ray microscopy has been demonstrated as a powerful tool to tackle challenges in these domains. X-ray chemical imaging can be realized via a spectromicroscopy approach, which utilizes the spectroscopic signals with spatial resolution to reveal the local chemistry (9, 10). The required energy resolution can be achieved either through energy-resolving detectors (11, 12) or through monochromatizing and scanning the energy of incident X-rays. A few different experimental modalities have been demonstrated to conduct X-ray imaging with compositional sensitivity at high resolution, including 1) K-edge differential and XANES imaging using a full-field transmission X-ray microscope (TXM) (9), 2) X-ray fluorescence (XRF) and X-ray diffraction (XRD) mapping with a scanning nanoprobe (5, 13), and 3) correlative XRF and transmission ptychographic imaging (14–16). These approaches clearly demonstrate a trade-off among detection sensitivity, spatial resolution, and experimental efficiency. Specifically, full-field transmission X-ray microscopy utilizes an area detector to resolve the transmitted X-rays spatially. Therefore, with a typical single-frame exposure time at the sub-second level, the throughput of full-field imaging is clearly superior to that of the scanning probes. The most time-consuming part of a full-field spectromicroscopy experiment is the energy tuning for the incident X-ray beam, which is typically executed through a physical rotation of the monochromator. Moreover, the recorded transmission signal features a strong, white-field background, leading to a relatively low detection sensitivity for this technique. On the other hand, the scanning nanoprobe typically utilizes a highly efficient, off-axis fluorescence detector to measure the spectrum of the sample's fluorescence emission induced by the X-ray excitation (5).

Author affiliations: [a]Stanford Synchrotron Radiation Lightsource, SLAC National Accelerator Laboratory, Menlo Park, CA 94025; [b]School of Data Science, City University of Hong Kong, Hong Kong, China; [c]X-ray Science Division, Argonne National Laboratory, Lemont, IL 60439; [d]Machine Learning Initiative, SLAC National Accelerator Laboratory, Menlo Park, CA 94025; [e]Department of Electronic Engineering, The Chinese University of Hong Kong, Hong Kong, China; and [f]Walker Department of Mechanical Engineering, The University of Texas at Austin, Austin, TX 78705

Author contributions: J.L., P.P., and Y.L. designed research; J.L., S.C., D.R., T.B., P.P., and Y.L. performed research; J.L., S.C., D.R., T.B., P.P., and Y.L. contributed new reagents/analytic tools; J.L. and Y.L. analyzed data; and J.L., S.C., D.R., T.B., P.P., and Y.L. wrote the paper.

The authors declare no competing interest.

This article is a PNAS Direct Submission.

[1]To whom correspondence may be addressed. Email: lijz@ieee.org or liuyijin@utexas.edu.

This article contains supporting information online at https://www.pnas.org/lookup/suppl/doi:10.1073/pnas.2314542120/-/DCSupplemental.

Published November 28, 2023.

The off-axis geometry makes the fluorescence detector effectively work in a "dark-field" mode, with the background suppressed to a very low level. In a scanning probe experiment, an image is built up pixel by pixel through raster scanning of the sample. Therefore, the imaging throughput is often considered a major limitation of this technique. Another challenge is that the desired tight X-ray focus is often associated with a low focusing efficiency, which could become a significant limitation for the throughput and the data quality. The recent development of simultaneous ptychography and XRF imaging utilizes the reconstructed X-ray probe profile to perform a numerical deconvolution to improve spatial resolution (15). It is effective to a certain extent; however, the experimental efficiency is still a major limitation, even with the projected synchrotron upgrades.

In this work, we report the development of a nanoscale X-ray structured-illumination chemical imaging technique (NxSCI), which combines the full-field transmission X-ray microscopy (TXM) with structured illumination and an X-ray fluorescence (XRF) detector to conduct elemental mapping of the sample with high efficiency. Along with a high-performance computational reconstruction algorithm, this single-pixel imaging scheme (17–19) enables nanoscale chemistry resolvability while eliminating the need for nanoscale X-ray focusing and raster scanning, both of which are indispensable in the conventional approach using a scanning probe. In general, single-pixel imaging operates by illuminating a sample with a series of varying patterns, with the integrated signal corresponding to each pattern captured by a single-pixel detector. Although the single-pixel detector does not provide spatial resolution by itself, the spatial information can be recovered through the correspondence to the illumination patterns. Furthermore, when the sample is sparse in some domain (e.g., regions of uniformity), compressive sensing methods leverage prior information about the sample to reconstruct samples using significantly fewer measurements than the number of pixels in the full-resolution image (17, 18, 20–22). We also note the close connection between the single pixel camera and the related concepts of multiplexing (23) and ghost imaging (19).

To assess the performance of the NxSCI method, we image a battery sample composed of mixed cathode materials and successfully retrieve the compositional variations in the imaged cathode particles. We compare our results to those obtained from traditional approaches through both numerical simulation and real experiments and highlight the advantages of our approach in terms of resolution, sensitivity, and imaging efficiency. Finally, we discuss current challenges and future perspectives of the NxSCI technique.

Results

Overview of the NxSCI Setup and Experimental Implementation. A schematic illustration of the developed NxSCI technique is shown in Fig. 1 (*Materials and Methods*), which consists of a customized X-ray microscope configuration with tunable illumination structures. It is followed by a computational reconstruction algorithm that uses the simultaneously acquired transmission patterns, TXM image, and XRF signals to reconstruct the elemental distribution within the sample. We implement this setup at beamline 6-2c of Stanford Synchrotron Radiation Lightsource (SSRL) for a proof-of-concept demonstration by leveraging and building upon the existing transmission X-ray microscope hardware. Specifically, two sandpaper diffusers with different grit sizes are inserted into the beam between the monochromator and capillary condenser to purposefully induce intensity inhomogeneity in the illumination with different spatial frequencies (*Discussion*). By independently scanning the

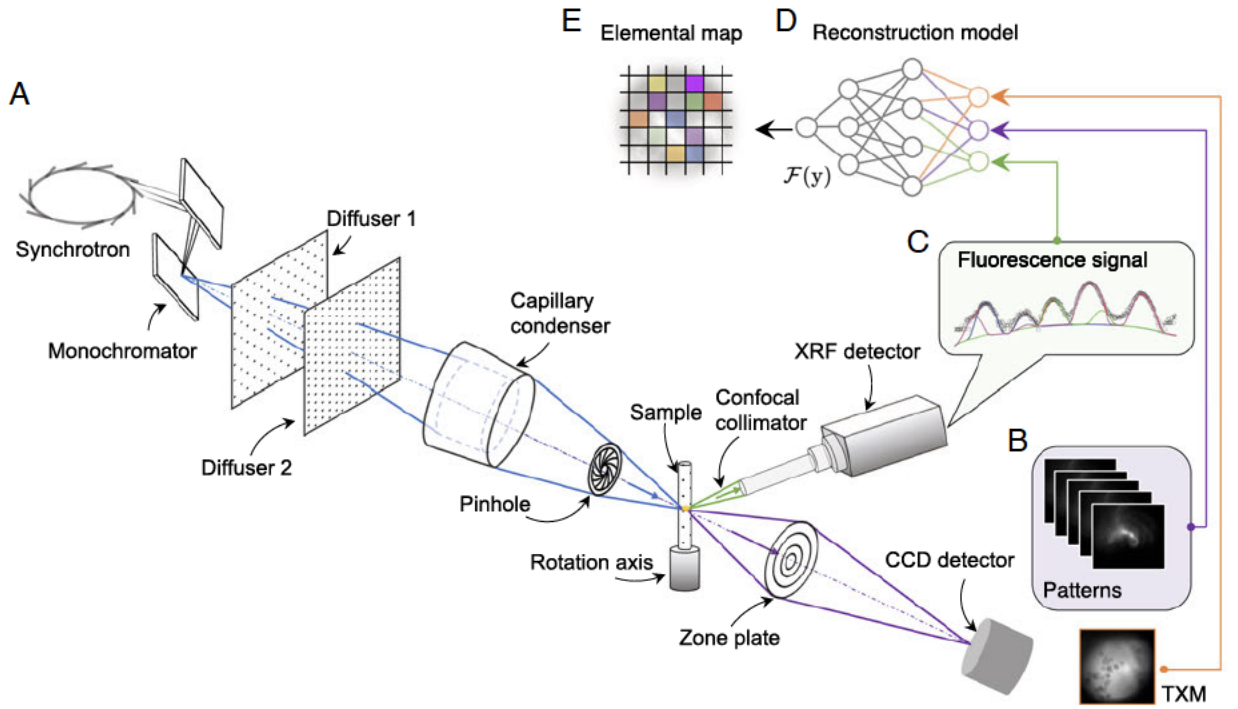

Fig. 1. Experimental setup and operation principle of the developed NxSCI technique for nanoscale chemical imaging with structured X ray illumination. (*A*) Two sandpaper diffusers are inserted into the X ray beam to modulate the illumination structures. (*B*) The corresponding patterns are recorded by a full field imaging detector downstream of the objective zone plate. (*C*) A Vortex XRF detector is used to collect the fluorescence signal on the fly. (*D*) The 1D fluorescence signal and 2D X ray illumination patterns are fed into an image reconstruction model to obtain the chemical elemental maps in (*E*).

two diffusers and by manipulating the microscope components, such as the condenser positions and angles, pinhole sizes, and zone plate positions, multiplexed X-ray illumination patterns can be effectively modulated and recorded on-the-fly. A few pictures of the modified TXM setup are given in *SI Appendix*, Fig. S1*A*. An energy-dispersive Vortex detector is placed perpendicular to the incident beam to collect the fluorescence signal from the sample. The illumination condition is adjusted within predefined ranges to minimize the time cost associated with motor movements. The fluorescence detector continuously records the XRF spectrum as the structured illumination conditions change. A confocal collimator is used to eliminate any background signals. It is worth pointing out that we have adopted an effective strategy to perform the data acquisition. Two transmission images, with and without the sample in place, are recorded for each illumination configuration, and the corresponding fluorescence signal is measured simultaneously. The limited sample stage precision and stability can cause potential errors in the correspondence between the illumination pattern (the sample-out image) and fluorescence signal. Thus, we have introduced a numerical image registration process to reflect the actual position of the illumination patterns. This on-the-fly pattern correlation scheme does not require the explicit splitting of the X-ray beam (24, 25), which is difficult to achieve in nanoscale synchrotron X-ray imaging. The structured illumination patterns, TXM image, and fluorescence signal are subsequently fed into the generative data reconstruction algorithm (*Materials and Methods*) to produce the spatially resolved composition maps of the sample.

Analysis of Structured Illumination Patterns. The quality of an illumination pattern set is critical to ensuring that the sample's morphological and chemical details across different length scales are sufficiently captured. Fig. 2*A* showcases a few examples of the experimentally recorded illumination patterns. Successful chemical map reconstruction heavily relies on and positively correlates with the level of independence in the pixels' intensity variations upon pattern change. For example, if the intensities over two different pixels are perfectly correlated, the level of independence between them is zero, and the recorded dataset does not contain any information that can separate these two pixels' respective contributions. Any difference in their respective chemical compositions will remain unresolved in this scenario. In contrast, a higher level of pixel independence will facilitate disentangling their contributions and, thus, improving the reconstruction quality and robustness.

To further illustrate this concept, we select three representative pixels and plot their normalized intensity variations upon pattern change in Fig. 2*B*. The similarity of the corresponding curves can evaluate the pattern correlation at these pixels. As demonstrated in Fig. 2*C*, the intensity at Position 2 (local illumination amplitude) exhibits a strong positive correlation with that at Position 1, while being more independent from that at Position 3. It suggests that the illumination at Positions 2 and 1 share similar characteristics, which is undesirable for the reconstruction process. As a comparison, in the point scanning approach, each pixel is either on or off, featuring 100% independence in the raster scan. In this case, the XRF signal sensed by the Vortex detector originates exclusively from one single illuminated pixel, as the other pixels receive no X-ray irradiation and are effectively "turned off" (*SI Appendix*, Fig. S2). Although the strong pixel independence in the "illumination patterns" of a point-scanning approach makes the image "reconstruction" straightforward, it becomes a major limitation regarding the experimental throughput and efficiency.

To evaluate the quality of an illumination pattern set, we define the dependence map (Fig. 2*D*) by calculating the Pearson correlation coefficients among different pixels in the field of view (FOV). We sort all the other pixels in the FOV for a certain target pixel based on their respective distances to the target (see Fig.2*A* for an illustration). This approach converts the calculated real-space map of the Pearson correlation coefficient into a vector. After iterating this process for all the pixels in the FOV, we construct a two-dimensional independence map in which the horizontal axis is the index of the target pixel, and each column represents the target's Pearson correlation coefficient vector (as described above). As we have discussed, a high level of pixel independence (blue color in the independence map) is desirable. When we add more patterns to a pattern set, an effective suppression of the large values (red color) in the independence map would indicate that the added new patterns carry new information and such additions are beneficial (Fig. 2*D*). The upper part of the independence map (pixels close to the target) generally exhibits a larger value, indicative of a lower level of independence. This is because most of the illumination patterns slowly vary, with a limited amount of high-spatial frequency features. This could become a limiting factor for the ultimate spatial resolution.

As an overall assessment of an illumination pattern set, the mean dependence value δ is calculated. Through analyzing the value of δ, we can assess the degree to which the pattern set exhibits statistical independence, providing a theoretical prediction on its effectiveness as input to the image reconstruction process. In a real-world experiment, as the number of effective measurements progressively increases, this pattern set's δ value is expected to decrease (Fig. 2*E*). However, the slope and saturation point can be quite different depending on the pattern configurations. As illustrated in Fig. 2*E*, the accumulation of patterns in two experiments exhibits diverging effects regarding independence improvement. This observation highlights the significance of designing the pattern set for high-efficiency and high-fidelity image reconstruction in our NxSCI approach. We further define invertibility as an indicator to evaluate the impact of illumination patterns on the reconstruction process (*SI Appendix*, Fig. S3). A higher invertibility indicates that the selected patterns contribute more effectively, improving overall performance when using the same number of patterns. Fig. 2*F* presents the comparative analysis of the invertibility of the two pattern sets, in which pattern set 2 clearly demonstrates superiority.

The differences in the independence and invertibility between these two pattern sets can be attributed to factors such as their underlying statistical properties, spatial distribution, and the intensities of the X-ray beams. By assessing these characteristics of the illumination patterns, we can determine their suitability for various imaging targets and conditions, allowing us to choose the most suitable sets to optimize and enhance the overall performance of our NxSCI approach. Moreover, carefully selecting suitable pattern sets enables us to continually optimize the acquisition strategy and improve efficiency when operating with a limited number of patterns or in challenging imaging conditions. Notably, pattern analysis and quantification can be conducted without the sample. This allows for an optimization of the experimental protocol prior to the actual experiment, thus causing no additional radiation dose to the sample.

Generative Image Reconstruction Model. The illumination patterns and the corresponding bulk fluorescence signal are fed into the generative reconstruction model $\mathcal{F}(\cdot)$ (*Materials and Methods*) to obtain the chemical map. Increasing the number

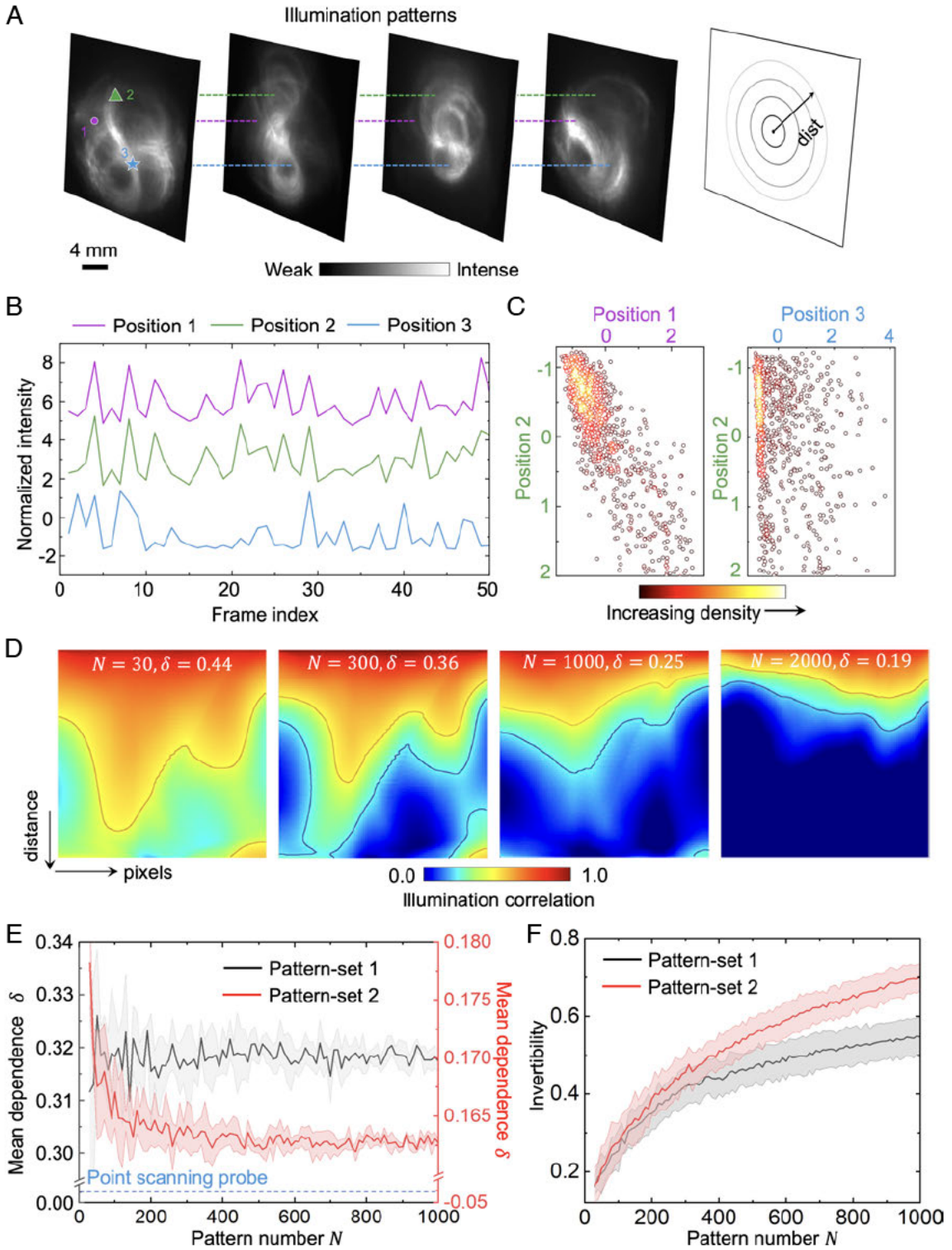

Fig. 2. Analysis of the structured illumination patterns. (*A*) Representative examples of the illumination patterns, which are generated by the effective modulation of the X ray imaging setup. (*B*) The normalized intensities at three positions in (*A*) from the NxSCI approach as a function of pattern indexes. (*C*) The scatter plots show the correlations between the intensity values at Position 2 and Positions 1 and 3. (*D*) The dependence maps of four sets of illumination patterns. Color represents the values of correlation coefficients. The pattern number (*N*) and mean dependence value δ are shown on the map. The "distance" quantifies the distance from the target pixel to the other pixels within the image field of view. (*E*) The mean dependences of two pattern sets as a function of pattern numbers. The ideal dependence $\delta = 0$ from the point scanning probe is represented as a line, indicating the optimal level of independence for the most accurate image reconstruction. (*F*) Comparison of the invertibility between two pattern sets for different numbers of illumination patterns.

of measurements with different illumination patterns can generally improve the reconstruction's accuracy by providing more information about the sample. It is thus essential to strike a balance between the number of patterns and the computational complexity of the reconstruction process. A properly designed reconstruction model could improve efficiency and robustness by generating good results from datasets with fewer illumination patterns. To evaluate the performance of the reconstruction

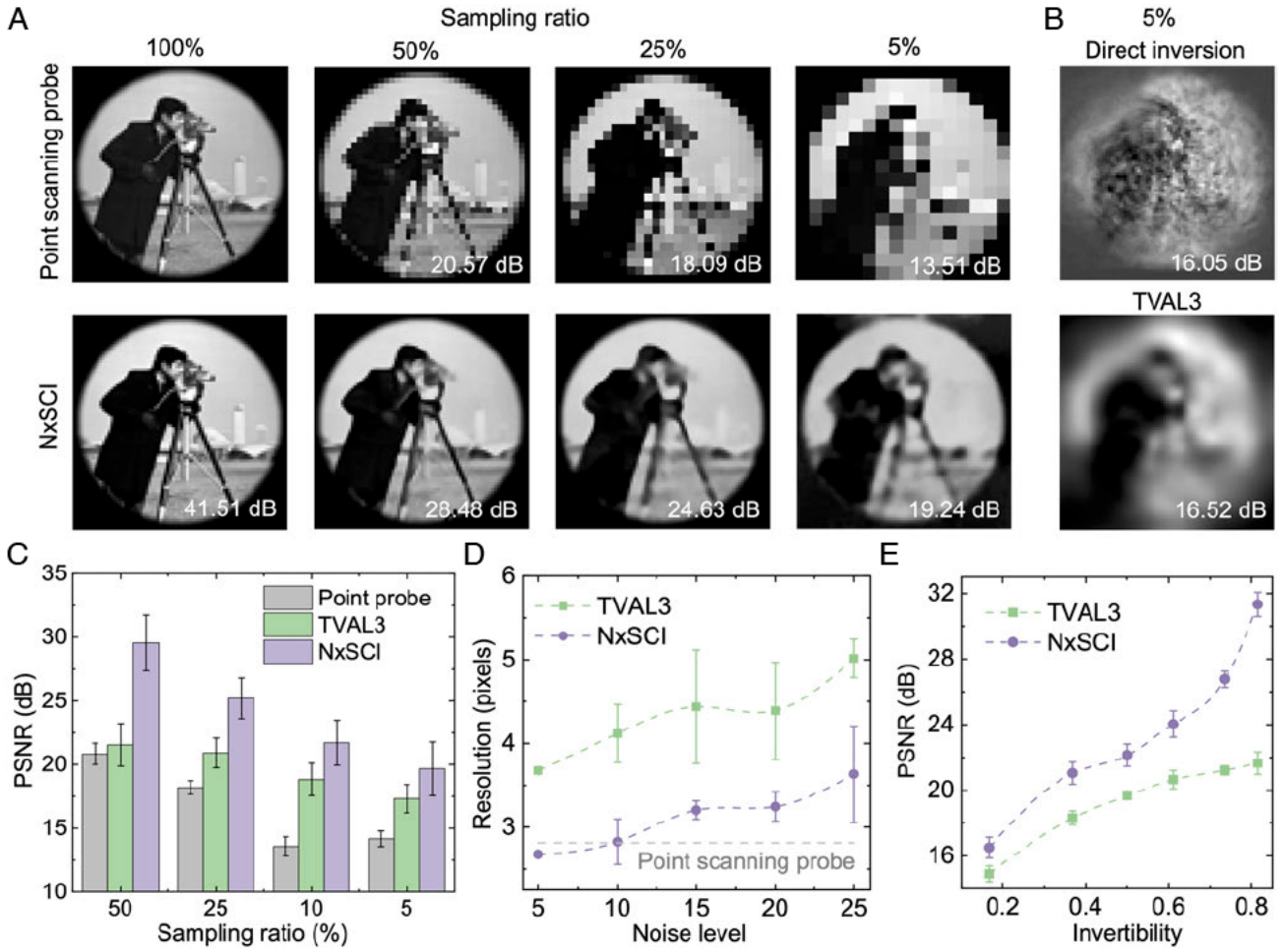

Fig. 3. Comparison of different reconstruction approaches with various sampling ratios and noise levels. (*A*) Comparison of the reconstructed images using the point scanning probe and the NxSCI approach for four different sampling ratios (100%, 50%, 25%, and 5%). The PSNRs are shown at the bottom of each image. (*B*) Reconstruction results from the direct inversion and TVAL3 (26) under the sampling ratio of 5%. (*C*) The reconstruction performance in terms of PSNR for different methods on different images under various sampling ratios. (*D*) The resolution of the reconstructed image from different algorithms as a function of the noise corruption levels. Smaller resolution indicates better reconstruction performance. Error bars represent the results from different noise realizations. (*E*) The relationship between the reconstruction PSNRs and the pattern invertibility. Error bars represent the results on different images.

model we developed for our NxSCI approach (*Materials and Methods* and *SI Appendix*, Fig. S4), we vary the sampling ratio (corresponding to different numbers of patterns in a pattern set) and compare the results with other reconstruction methods through simulations.

We first compare the reconstructed results from our NxSCI method to those from a conventional point scanning approach. In Fig. 3*A*, the reconstructed images under four different sampling ratios, 100%, 50%, 25%, and 5% (corresponding to 6,400, 3,200, 1,600, and 320 measurements with different illumination patterns, respectively) are presented. PSNR (peak signal-to-noise ratio) values are calculated and shown at the bottom of each image. As expected, it is difficult to recover the image details accurately when the sampling ratio is low. Compared with the point probe approach, our reconstructed results by the NxSCI approach demonstrate a noticeably higher quality. The advantages of our approach are more significant when the sampling ratio is low.

We further compare our reconstruction method against two typical reconstruction models, direct inversion and TVAL3 (26). Direct inversion refers to a straightforward mathematical method for reconstructing the image from the acquired measurements by directly inverting the sensing matrix (implemented as the Moore–Penrose pseudoinverse) to obtain an estimate of the original image. The TVAL3 algorithm combines the benefits of Total Variation minimization with the Augmented Lagrangian and Alternating Direction Methods of Multipliers framework, making it a popular choice for a wide range of linear inverse problems (27–30), particularly in single-pixel compressive imaging techniques which involve random illumination patterns (17, 18, 31, 32). As shown in Fig. 3*B*, for a 5% sampling case, the direct inversion failed to reconstruct since the sensing matrix is ill-conditioned properly. TVAL3 cannot retrieve the image details either when the sampling ratio is low and introduces significant artifacts in the reconstructed image. A quantitative comparison of PSNR values from different algorithms across various sampling ratios is shown in Fig. 3*C*. We also compare the resolution of the reconstructed images from different methods by calculating the Fourier ring correlation (FRC) with the ground truth images (33) (*Materials and Methods* and *SI Appendix*, Fig. S5). In addition, the noise robustness of image reconstruction is evaluated, and the results are shown in Fig. 3*D*. More comparisons can be found in *SI Appendix*, Fig. S6.

Overall, the developed reconstruction model serves our nanoscale chemical imaging technique very well, demonstrating a superior performance in terms of various image quality metrics

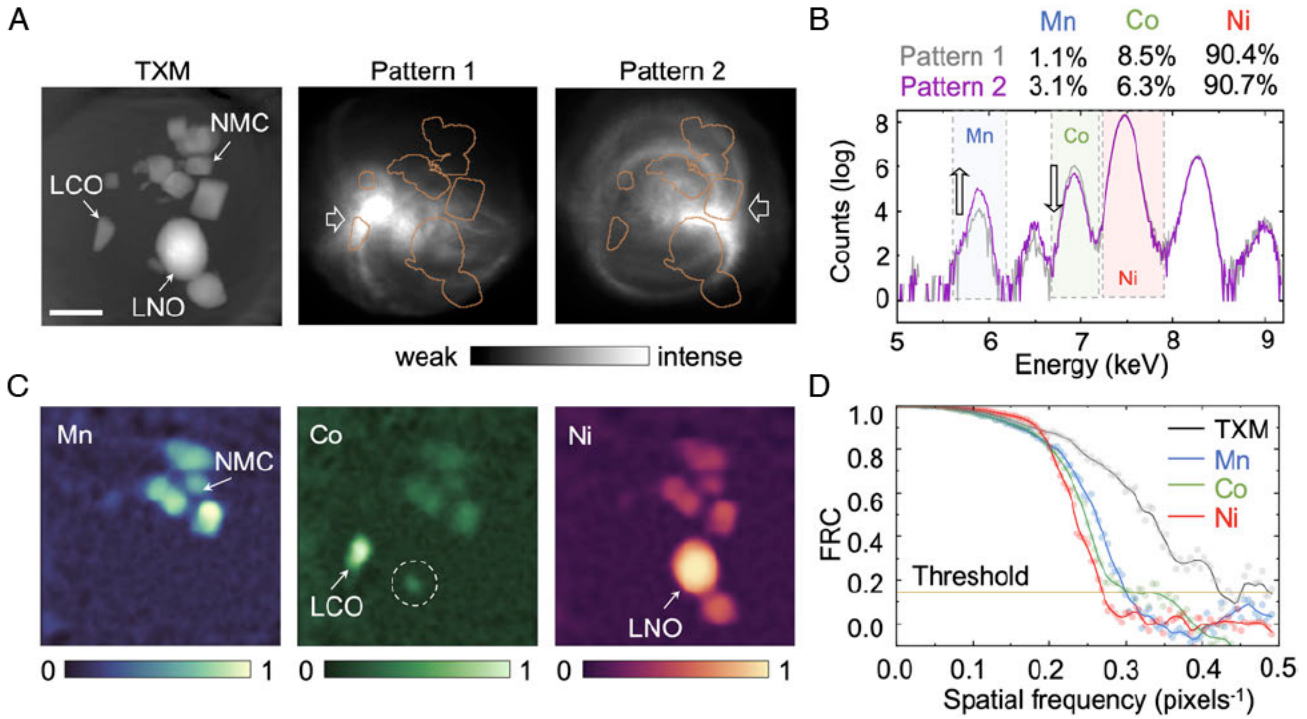

Fig. 4. Reconstruction of elemental distribution in a lithium battery sample with mixed cathode material. (*A*) TXM image of the sample containing LCO, NMC, and LNO. Two representative illumination patterns are shown on the *Right*. The object boundaries extracted from the TXM image overlay the illumination patterns. (*B*) The fitted percentage changes of the elements of interest, e.g., Mn, Co, and Ni, under the illumination of the patterns in (*A*). (*C*) The reconstructed concentration maps of Mn, Co, and Ni. The white dotted circle highlights a small piece of LCO particle attaching to the surface of a larger LNO particle. (*D*) Resolution quantification based on FRC analysis for the reconstructed elemental maps and compared with that of the TXM image (threshold 0.143). The scale bar in (*A*) is 5 μm.

and robustness. We also evaluate the relationship between the pattern set's invertibility and the reconstruction performance. Fig. 3*E* demonstrates a clear relationship between the PSNRs and the invertibility of the illumination pattern set. As the invertibility increases, the PSNR values increase, indicating a positive correlation between these two factors. This observation supports the need to select a set of illumination patterns with higher invertibility, leading to better reconstruction performance.

It is worth pointing out that although fine features in the illumination pattern are intuitively desirable, the most effective illumination pattern set's feature size could vary, depending on the targeted sample. To elaborate on this point, we provide the reconstruction results of the developed reconstruction model under illumination pattern sets with different feature sizes in *SI Appendix*, Fig. S7. We start from a set of completely random patterns and gradually reduce the spatial frequency by conducting 2D Gaussian filtering with a growing kernel. The simulation result shows that the best performance is achieved by a pattern set with many features matching the level of detail in the sample. These results showcase the generality and adaptability of our reconstruction model, demonstrating its robustness and reliability across a range of situations. It highlights the importance of joint optimization of algorithm design and experimental generation of illumination patterns.

Elemental Mapping of Composite Lithium-Ion Battery Cathode. Resolving compositional heterogeneities of lithium-ion battery materials is essential for thoroughly understanding battery reactions, degradation, and failure (34, 35). We apply the developed NxSCI technique to image a battery sample with mixed cathode particles as a proof-of-concept demonstration.

Specifically, the imaged battery sample (Fig. 4*A*) consists of three types of cathode particles, $LiNi_{0.7}Mn_{0.2}Co_{0.1}O_2$ (NMC), $LiCoO_2$ (LCO), and $LiNiO_2$ (LNO). They are mixed randomly, and their morphologies can be observed using scanning electron microscopy (*SI Appendix*, Fig. S8). The structured illumination patterns employed in the NxSCI approach effectively weigh different parts of the sample differently, encoding the compositional heterogeneity into the fluorescence signals. We extract the areas of Mn, Co, and Ni elements by fitting XRF spectra (*Materials and Methods*). The experiments were conducted with an X-ray incident photon energy of 9 keV, and each TXM image was collected with a data acquisition time of 0.5 s. We would like to clarify that, although the TXM's objective zone plate has limited focusing optics, in our configuration, the XRF detector is placed upstream of the zone plate and its efficiency and throughput are not affected by the photon loss downstream of the sample. In our reconstruction process, we essentially use the patterns and the associated XRF spectra. This can be done separately if the stages can provide sufficient positioning reproducibility. The illumination patterns can be acquired before the sample is exposed to the X-ray beam. This can be viewed as a system calibration protocol. If this is done properly, when the sample is subjected to the XRF measurements, the experimental throughput and dose efficiency can be significantly improved. As shown in Fig. 4*B*, the change in illumination pattern leads to changes in the XRF signals, which can be decoded later using our reconstruction algorithm described above. A representative example of the measured XRF spectrum, its fitted data, and the spectrum of different chemical elements is shown in *SI Appendix*, Fig. S9*A*. The percentages of Mn, Co, and Ni, and the fitted areas for different illumination patterns are shown in *SI Appendix*, Fig. S9 *B*–*E*, respectively. We should point

out that, in the NxSCI implementation, the XRF detector integrates fluorescence signals from the illuminated sample without intrinsically offering any spatial resolution. The structured illumination-enabled encoding/decoding process offers the opportunity to resolve the distribution of elements of interest spatially.

The extracted amplitude of each element and the measured illumination patterns ($N = 1{,}000$) are fed into the reconstruction model, and the resulting elemental maps are shown in Fig. 4*C*. As observed, the spatial distributions and concentrations of different elements within the sample are faithfully retrieved through the developed NxSCI technique. The correlations between different elements are given in *SI Appendix*, Fig. S10, which helps identify the cathode species in which different elements of interest could co-exist. We further quantify the FRCs of the reconstructed elemental maps. As shown in Fig. 4*D*, the resolutions of these chemical maps are slightly lower than that of the TXM image by a factor of 1.5 to 2, at the level of 100 nm, highlighting the potential of the NxSCI technique to achieve nanoscale spatially resolved chemical imaging and open up broad avenues for material characterization and development with tailored functionalities.

Discussion

This work presents a nanoscale chemical X-ray imaging technique that employs structured illumination to enable high-resolution, high-efficiency, spatially resolved mapping of elemental distributions within a sample. By jointly optimizing the illumination scheme and the image reconstruction model, the developed NxSCI approach overcomes the limitations of traditional XRF point scanning probes, which are time-consuming for several reasons, including the limited X-ray focusing efficiency and the required mechanical raster scan. Our method demonstrates superior image quality, especially when working with significantly under-sampled datasets. We validate the effectiveness and performance of the NxSCI approach using a lithium-ion battery sample with mixed cathode particles. The results highlight the potential of NxSCI in addressing real-world challenges in characterizing complex materials and showcasing its versatility. The following sections further discuss this method's significance, uniqueness, applicability, and limitations.

Generating nanoscale, spatially resolved elemental maps of a sample with a synchrotron micro/nano-probe beamline typically involves the use of X-ray focusing optics, implementation of the high-precision sample raster scan, and acquisition of the XRF signals with a Vortex detector. The effective spatial resolution of a scanning probe experiment can be affected by the X-ray focal size, pixel dwell time, signal-to-noise ratio, elemental concentrations, as well as the sample's micromorphology and surface topography, etc. Efforts have been devoted to improving the imaging field-of-view, scanning efficiency, sensitivity, and spatial resolution (5, 36, 37). However, significant technical challenges persist. For example, when X-ray nano-focusing optics are required for high-resolution mapping, their design, fabrication, aberration correction, and positioning are rather complex and expensive. A tight X-ray focus inevitably comes at the cost of a lower flux due to the limited focusing efficiency, negatively affecting the experimental throughput. As we approach nano-resolution, the engineering challenge increases dramatically in positioning and scanning the optics and samples with high precision, stability, and reproducibility. Another general concern in X-ray microscopy is associated with the X-ray dose and dose rate, both of which have detrimental effects on various samples. This leads to the need to implement cryogenic sample environments, for example, in biology research, which is not ideal in many scenarios.

The developed NxSCI technique overcomes these limitations by utilizing a structured illumination scheme integrated with a generative image reconstruction model to obtain the elemental maps. This approach enables high-resolution XRF mapping with the elimination of complex nano-focusing optics and high-precision positioning systems, making it accessible, cost-effective, and highly efficient even with a similar order of measurement points as traditional methods. There are some limitations in the current implementation of our method. Specifically, the limited sample stage accuracy necessitates the acquisition of image pairs with and without the sample under different illumination patterns. The experimental throughput can be significantly improved with the use of high-precision stages, which could allow us to configurate the system and to optimize the data acquisition protocol prior to exposing the sample of interest to the X-rays. We utilize sandpapers as beam diffusers to generate the desired random illumination patterns. The sandpapers are coupled with the capillary condenser in a demagnification geometry, yielding nanoscale, structured illumination patterns at essentially zero cost (instead of creating nano-sized and high-aspect-ratio structures through nanofabrication methods). However, we should point out that, with the use of sandpapers, it is impossible to design illumination patterns in a deterministic manner purposely. This is due to the complex scattering process through the physical structure of the sandpaper. On the other hand, with this approach, it is possible to directly exploit the randomness of the scattering process and solve an inverse problem to reconstruct the image carried by the signal, which is one of the key contributions of the developed method.

We evaluate the quality of the illumination scheme by calculating the patterns' independence and invertibility in terms of image reconstruction quality and robustness against different levels of noise and undersampling. By analyzing these characteristics, we formulate a predictive metric that can guide the optimization of the illumination scheme to enhance the overall performance of this technique. In practice, this can be achieved by selecting sandpapers with various grit sizes, tuning the beamline and endstation optics, and adjusting the exposure time dynamically. The goal of this illumination scheme optimization is to ensure a sufficient sampling of the sample with a minimized number of measurements.

It is useful to compare several of the relevant X-ray imaging modalities from the dose efficiency perspective. In a scanning probe approach, the photon loss due to limited focusing efficiency occurs upstream of the sample and, therefore, it would not add any unnecessary dose to the sample. In the conventional full-field TXM approach, however, the objective zone plate is placed downstream of the sample and its limited focusing efficiency would lead to a reduction in the overall dose efficiency. This is because, in traditional TXM configuration, some of the photons that transmit through the sample and carry useful information about the sample cannot be collected by the zone plate and thus cannot contribute to the signal on the imaging detector in the downstream. In the herein proposed approach, the off-axis XRF detector is placed upstream of the TXM's objective zone plate. The objective zone plate–induced photon loss does not affect the XRF intensity and efficiency in our configuration. For efficiency of the fluorescence signal detection, one important aspect to consider is the coverage of solid angle, which can be enlarged by placing the XRF detector very close to the sample. This is similar in the scanning probe configuration and the existing optimization

processes developed for the scanning probes are applicable and can be leveraged.

The generative image reconstruction model in the developed NxSCI technique is constructed by self-supervised learning the continuous image representation parameterized by a coordinate-based neural network (38, 39). It provides an effective and robust method for image reconstruction from compressive measurements by leveraging the prior knowledge from the transmission image with a flat-field illumination. Including a customized loss function within this model significantly enhances the overall performance of the NxSCI approach. By simulating the image formulation process, we evaluate the performance of the reconstruction model by assessing the impact of sampling ratios, noise, and different illumination patterns and comparing it with other state-of-the-art algorithms for solving similar inverse problems.

NxSCI's significance lies in its potential to revolutionize nanoscale elemental mapping using X-rays by offering a more efficient and accurate method for reconstructing high-resolution and spatially resolved XRF signals. Its applicability spans various research domains, including materials science, geology, and biological sciences. Although superior resolvability has been demonstrated, in the current implementation, the effective spatial resolution is at a level of over 100 nm and is limited by the critical feature size available in the illumination patterns and presented errors in the acquisition systems. The upgrade/construction of next-generation synchrotron facilities with unprecedented transversal coherence will be able to generate speckle illumination patterns with higher spatial frequency, which could effectively improve the spatial resolution of our NxSCI reconstruction.

We highlight the flexibility of the implemented framework in this study, as it provides room for further improvements. For instance, adding an on-the-fly pattern assessment module could facilitate autonomous experimentation with NxSCI. This would streamline the process and further increase efficiency, potentially leading to broader applications and improvements in future works. While the current implementation of NxSCI is primarily focused on 2D imaging, expanding this technique to 3D volumetric elemental mapping represents a promising direction for future research. This can be achieved by rotating the sample stage to capture images from different angles, then applying a tomographic reconstruction step. It is worth pointing out that while the current demonstration focuses on mapping elemental composition, the capability of NxSCI can be further extended to intricately differentiate different chemical states and/or lattice configurations. To achieve this, further efforts are needed in the incorporation of various detectors, refining of illumination patterns, and improving of the image reconstruction algorithms.

Additionally, in the context of laboratory X-ray sources, where photon flux is a precious resource, employing sandpaper as a diffuser may not be the most suitable option. Alternatives for generating structured patterns might need to be considered. For example, our previous collaborative development of a Transverse Lighting Interface (TLI) system equipped with a microarray anode-structured target (MAAST) source (40) could be a promising solution for producing structured illumination patterns in the laboratory.

Materials and Methods

In the proposed NxSCI technique, the data acquisition pipeline involves generating structured illumination patterns, scanning the sample, detecting the emitted XRF signals, and extracting the composition of chemical elements for further reconstruction. By associating specific structured illumination patterns with individual elemental fitted areas, the modified coordinate-based generative neural network effectively learns and recreate the spatial distributions of different chemical elements within the sample.

Pattern Alignment and Evaluation. To effectively correct errors in the correspondence between the illumination pattern and fluorescence signal due to limited sample stage precision and stability, we use the transmission image of the sample (TXM) as a reference and apply the phase correlation algorithm to find the translation of the illumination pattern with and without the sample in place.

The mean dependence δ of a sensing matrix $A \in \mathbb{R}^{N\times M}$ is defined as the average values of the Pearson correlation coefficient between two distinguished rows of A:

$$\delta = \underset{1\le i\neq j\le N}{\text{Mean}} \frac{\text{cov}(A_i, A_j)}{\sigma_{A_i}\sigma_{A_j}},$$

where $M = M_x \times M_y$ is the total pixel number of one single image frame, and N is the number of illumination patterns. $\text{cov}(A_i, A_j)$ is the covariance, σ_{A_i} and σ_{A_j} represents the SD of A_i and A_j, respectively. A smaller value of δ indicates larger pixel independence between different illumination patterns, thus having positive effects on the reconstruction quality and robustness.

The invertibility of the illumination pattern set is defined as the structural similarity index (SSIM) value (41) between the reconstructed image by Moore–Penrose pseudoinverse-based method and the ground truth image (*SI Appendix*, Fig. S3). The singular value decomposition is used for the calculation. The resultant invertibility is a decimal value between −1 and 1, where 1 indicates perfect invertibility and larger is better.

XRF Spectrum Collection and Analysis. During the XRF signal acquisition process, the Vortex detector stage is adjusted in order to obtain the maximum intensity of the XRF signal while simultaneously minimizing background noise. Customized scripts are developed and integrated to control the movements of motors, beamline settings, TXM image capturing, and XRF signal collection sequentially. All spectra are analyzed by the software PyMCA (42), developed by European Synchrotron Radiation Facility (ESRF). The fitted areas for each predefined element, coupled with the corresponding illumination patterns, serve as the primary inputs for the reconstruction process.

Image Formation Model and Proposed Reconstruction Approach. We consider the data formulation model following the single-pixel imaging framework (17, 18). The object of interest is denoted as $\mathrm{x} \in \mathbb{R}^{M\times 1}$, which is a vectorized form of the two-dimensional chemical element distribution of the sample with pixel number M. The measurement matrix $A \in \mathbb{R}^{N\times M}$ represents the structured illumination patterns, where each row corresponds to a vectorized version of a specific pattern. The measurement $\mathrm{y} \in \mathbb{R}^{N\times 1}$ representing the intensity of fluorescence signal of a specific chemical element for all N illumination patterns can be described as:

$$\mathrm{y} = A\mathrm{x} + \mathrm{b},$$

where the vector $\mathrm{b} \in \mathbb{R}^{N\times 1}$ denotes the measurement errors and other uncertainties in the data acquisition and analysis process, e.g., the unwanted background contamination or the XRF fitting errors, etc. Through this way, the problem of reconstructing the chemical element distribution x is transformed into the problem of solving M independent unknowns by using N linear equations. One solution to this problem can be obtained by the direct matrix inversion $\hat{\mathrm{x}} = A^{-1}\mathrm{y}$. However, this solution is sensitive to noise and suboptimal since the problem is ill-posed, and the number of measurements is often much smaller than the number of unknowns ($N \ll M$).

Various computational methods can be employed to solve this problem, such as compressive sensing (43), optimization-based iterative algorithms (44), or deep learning methods (45–48). These algorithms typically leverage the sparsity or other prior knowledge from the training dataset about the object x to achieve accurate reconstructions from a limited number of measurements. For example, based on total variation (TV) regularization promoting sparsity

in the gradient domain of the image, the TVAL3 algorithm (26) is a fast and effective algorithm for solving such an image reconstruction problem. It is worth mentioning that most of the current developments in single-pixel imaging are based on random speckle illumination patterns due to their low mutual coherence, universality, and simplicity. However, generating deterministic nanoscale illumination patterns is difficult without nanoscale focusing optics and fabrication. In addition, many algorithms divide the signal into smaller non-overlapping or overlapping patches and then reconstruct each patch separately, given the assumption that their sensing matrixes are invariant for different patches, which does not hold in the NxSCI setting.

In this work, we propose a self-supervised generative approach to obtain the continuous representation of the elemental maps to solve this inverse problem. The goal is to identify a set of optimal weights θ for the neural network such that when the measurements matrix A is applied to the network output, it aligns closely with the measurements y acquired from the experiments. We achieve this by leveraging the implicit neural representation (38, 39, 49, 50) to parameterize the spatial coordinates $\mathrm{z} = (c_i, c_j)$, effectively mapping the image, i.e., $\mathrm{x} = f_\theta(\mathrm{z})$. The neural network architecture uses multi-layer perceptrons (MLP) with the sine as a periodic activation function (50); that is, the i-th layer of the network can be represented as

$$\phi_i(\mathrm{z}) = \sin\left(\omega_i * \mathrm{W}_i\phi_{i-1}(\mathrm{z}) + \beta_i\right),$$

where w_i is the frequency of the i-th layer, W_i and β_i are the weight and bias of the i-th layer, respectively. $\phi_{i-1}(\cdot)$ is the previous layer's output (or the input coordinates for $i = 1$). Due to the ill-posedness of this problem, we leverage prior knowledge from the TXM image in the NxSCI setting and incorporate it into our cost function as a regularization term. Inspired by the annihilation-driven image approximation (51), we encourage the gradients of the output image (i.e., the edge information) from our network to match those of the TXM image as closely as possible. Given that the input to the neural network is the spatial coordinates, the trained network essentially forms a continuous representation of the elemental maps. This continuous representation lends itself well to scalability, allowing for reconstructing large-scale images by feeding the network with appropriate coordinate inputs, corresponding illumination patterns, and XRF signals.

Thus, the image reconstruction problem can be formulated mathematically as follows:

$$\hat{\mathrm{x}} = f_{\hat{\theta}}(\mathrm{z}), \hat{\theta} = \underset{\theta}{\operatorname{argmin}} \|Af_\theta(\mathrm{z}) - \mathrm{y}\|_2^2 + \lambda\|\nabla f_\theta(\mathrm{z}) - \nabla I\|_1.$$

Here, $\nabla f_\theta(\mathrm{z})$ represents the gradient of the estimated image, ∇I is the gradient of the TXM image $I \in \mathbb{R}^{M_x \times M_y}$, and λ is a regularization parameter. By adjusting the regularization parameter, we can balance the fidelity of the reconstruction to the compressive measurements and its consistency with the structural TXM image. Note that appropriate thresholding for noise suppression can be applied to ∇I to achieve better reconstruction performance. For the training process, we utilize the Adam optimizer for all experiments in this work. A schematic illustration of the reconstruction model is given in *SI Appendix*, Fig. S4.

Image Quality Assessment and Resolution Measure. We majorly assess the quality of the image reconstruction by the peak signal-to-noise ratio (PSNR), which is a common measure that calculates the ratio between the maximum possible power of the signal and the power of the corrupting noise. Higher PSNR values generally indicate better reconstruction. The image resolution is measured by FRC (33), which is based on a normalized cross-correlation histogram computed in the frequency domain between two images. We use the ImageJ plugin for the calculation, and the fixed 1/7 resolution threshold (52) is used to determine the numerical resolution value.

Data, Materials, and Software Availability. Source code is deposited in the GitHub repository (https://github.com/YijinLiu-Lab/NxSCI) (53). All other data are included in the manuscript and/or *SI Appendix*.

ACKNOWLEDGMENTS. The work at SLAC National Accelerator Laboratory is supported by the Department of Energy, Laboratory Directed Research and Development program under contract DE-AC02–76SF00515. The engineering support from D. Van Campen, D. Day, and V. Borzenets for the transmission X-ray microscopy experiment at beamline 6-2C of Stanford Synchrotron Radiation Lightsource is gratefully acknowledged.

1. J. F. Collingwood, F. Adams, Chemical imaging analysis of the brain with X-ray methods. *Spectrochim. Acta, Part B* **130**, 101–118 (2017).
2. R. F. Egerton, *Electron Energy-Loss Spectroscopy in the Electron Microscope* (Springer US, Boston, MA, 2011).
3. D. Kurouski, A. Dazzi, R. Zenobi, A. Centrone, Infrared and Raman chemical imaging and spectroscopy at the nanoscale. *Chem. Soc. Rev.* **49**, 3315–3347 (2020).
4. F. Lin *et al.*, Synchrotron X-ray analytical techniques for studying materials electrochemistry in rechargeable batteries. *Chem. Rev.* **117**, 13123–13186 (2017).
5. A. Pattammattel *et al.*, High-sensitivity nanoscale chemical imaging with hard X-ray nano-XANES. *Sci. Adv.* **6**, eabb3615 (2020).
6. S. Rizvi *et al.*, *Handbook of Semiconductor Manufacturing Technology* (CRC Press, Boca Raton, FL, ed. 2, 2007).
7. C. Tian *et al.*, Charge heterogeneity and surface chemistry in polycrystalline cathode materials. *Joule* **2**, 464–477 (2018).
8. J. Wang, Ed., *Advanced X-ray Imaging of Electrochemical Energy Materials and Devices* (Springer, Singapore, 2021).
9. F. Meirer *et al.*, Three-dimensional imaging of chemical phase transformations at the nanoscale with full-field transmission X-ray microscopy. *J. Synchrotron Radiat.* **18**, 773–781 (2011).
10. J. Wang, Y.-C. Karen Chen-Wiegart, C. Eng, Q. Shen, J. Wang, Visualization of anisotropic–isotropic phase transformation dynamics in battery electrode particles. *Nat. Commun.* **7**, 12372 (2016).
11. R. G. Castillo *et al.*, High-energy-resolution fluorescence-detected X-ray absorption of the Q intermediate of soluble methane monooxygenase. *J. Am. Chem. Soc.* **139**, 18024–18033 (2017).
12. S. Friedrich, Cryogenic X-ray detectors for synchrotron science. *J. Synchrotron Radiat.* **13**, 159–171 (2006).
13. R. P. Winarski *et al.*, A hard X-ray nanoprobe beamline for nanoscale microscopy. *J. Synchrotron Radiat.* **19**, 1056–1060 (2012).
14. K. W. Bossers *et al.*, Correlated X-ray ptychography and fluorescence nano-tomography on the fragmentation behavior of an individual catalyst particle during the early stages of olefin polymerization. *J. Am. Chem. Soc.* **142**, 3691–3695 (2020).
15. J. Deng *et al.*, Correlative 3D X-ray fluorescence and ptychographic tomography of frozen-hydrated green algae. *Sci. Adv.* **4**, eaau4548 (2018).
16. J. Deng *et al.*, Simultaneous cryo X-ray ptychographic and fluorescence microscopy of green algae. *Proc. Natl. Acad. Sci. U S.A.* **112**, 2314–2319 (2015).
17. M. P. Edgar, G. M. Gibson, M. J. Padgett, Principles and prospects for single-pixel imaging. *Nat. Photonics* **13**, 13–20 (2019).
18. G. M. Gibson, S. D. Johnson, M. J. Padgett, Single-pixel imaging 12 years on: A review. *Opt. Express* **28**, 28190–28208 (2020).
19. T. J. Lane, D. Ratner, What are the advantages of ghost imaging? Multiplexing for X-ray and electron imaging. *Opt. Express* **28**, 5898–5918 (2020).
20. B. Sun *et al.*, 3D computational imaging with single-pixel detectors. *Science* **340**, 844–847 (2013).
21. C. M. Watts *et al.*, Terahertz compressive imaging with metamaterial spatial light modulators. *Nat. Photonics* **8**, 605–609 (2014).
22. R. I. Stantchev, Yu. Xiao, T. Blu, E. Pickwell-MacPherson, Real-time terahertz imaging with a single-pixel detector. *Nat. Commun.* **11**, 2535 (2020).
23. N. J. Sloane, Multiplexing methods in spectroscopy. *Math. Mag.* **52**, 71–80 (1979).
24. D. Pelliccia, A. Rack, M. Scheel, V. Cantelli, D. M. Paganin, Experimental X-ray ghost imaging. *Phys. Rev. Lett.* **117**, 113902 (2016).
25. Yu. Hong *et al.*, Fourier-transform ghost imaging with hard X rays. *Phys. Rev. Lett.* **117**, 113901 (2016).
26. C. Li, W. Yin, H. Jiang, Y. Zhang, An efficient augmented Lagrangian method with applications to total variation minimization. *Comput. Optim. Appl.* **56**, 507–530 (2013).
27. Z. Gao *et al.*, Single-pixel imaging with Gao–Boole patterns. *Opt. Express* **30**, 35923–35936 (2022).
28. G. Haberfehlner *et al.*, Formation of bimetallic clusters in superfluid helium nanodroplets analysed by atomic resolution electron tomography. *Nat. Commun.* **6**, 8779 (2015).
29. C. Li, T. Sun, K. F. Kelly, Y. Zhang, A compressive sensing and unmixing scheme for hyperspectral data processing. *IEEE Trans. Image Process.* **21**, 1200–1210 (2012).
30. Yu. Xiao, R. I. Stantchev, F. Yang, E. Pickwell-MacPherson, Super sub-Nyquist single-pixel imaging by total variation ascending ordering of the Hadamard basis. *Sci. Rep.* **10**, 9338 (2020).
31. J. Liang, L. V. Wang, Single-shot ultrafast optical imaging. *Optica* **5**, 1113–1127 (2018).
32. M. Lyu *et al.*, Deep-learning-based ghost imaging. *Sci. Rep.* **7**, 17865 (2017).
33. R. P. J. Nieuwenhuizen *et al.*, Measuring image resolution in optical nanoscopy. *Nat. Methods* **10**, 557–562 (2013).
34. F. Lin, K. Zhao, Y. Liu, Heterogeneous reaction activities and statistical characteristics of particle cracking in battery electrodes. *ACS Energy Lett.* **6**, 4065–4070 (2021).
35. M. Linqin *et al.*, Resolving charge distribution for compositionally heterogeneous battery cathode materials. *Nano Lett.* **22**, 1278–1286 (2022).
36. N. P. Edwards *et al.*, A new synchrotron rapid-scanning X-ray fluorescence (SRS-XRF) imaging station at SSRL beamline 6-2. *J. Synchrotron Radiat.* **25**, 1565–1573 (2018).
37. H. Mimura *et al.*, Breaking the 10 nm barrier in hard-X-ray focusing. *Nat. Phys.* **6**, 122–125 (2010).
38. B. Mildenhall *et al.*, NeRF: Representing scenes as neural radiance fields for view synthesis. *Commun. ACM* **65**, 99–106 (2021).

39. M. Tancik *et al*., "Fourier features let networks learn high frequency functions in low dimensional domains" in *34th Conference on Neural Information Processing Systems* (IEEE, Vancouver, Canada, 2020), pp. 7537–7547.
40. G. Zan *et al*., High-resolution multicontrast tomography with an X-ray microarray anode-structured target source. *Proc. Natl. Acad. Sci. U S.A.* **118**, e2103126118 (2021).
41. Z. Wang, A. C. Bovik, H. R. Sheikh, E. P. Simoncelli, Image quality assessment: From error visibility to structural similarity. *IEEE Trans. Image Process.* **13**, 600–612 (2004).
42. V. A. Solé, E. Papillon, M. Cotte, P. Walter, J. Susini, A multiplatform code for the analysis of energy-dispersive X-ray fluorescence spectra. *Spectrochim. Acta, Part B* **62**, 63–68 (2007).
43. M. F. Duarte *et al*., Single-pixel imaging via compressive sampling. *IEEE Signal Process. Mag.* **25**, 83–91 (2008).
44. Y. Wang, J. Yang, W. Yin, Y. Zhang, A new alternating minimization algorithm for total variation image reconstruction. *SIAM J. Imag. Sci.* **1**, 248–272 (2008).
45. C. F. Higham, R. Murray-Smith, M. J. Padgett, M. P. Edgar, Deep learning for real-time single-pixel video. *Sci. Rep.* **8**, 2369 (2018).
46. F. Wang, C. Wang, C. Deng, S. Han, G. Situ, Single-pixel imaging using physics enhanced deep learning. *Photonics Res.* **10**, 104–110 (2022).
47. Y. Yang, J. Sun, H. Li, X. Zongben, ADMM-CSNet: A deep learning approach for image compressive sensing. *IEEE Trans. Pattern Anal. Mach. Intell.* **42**, 521–538 (2020).
48. J. Zhang, B. Ghanem, "ISTA-Net: Interpretable optimization-inspired deep network for image compressive sensing" in *2018 IEEE/CVF Conference on Computer Vision and Pattern Recognition* (IEEE, Salt Lake City, UT, 2018), pp. 1828–1837.
49. V. Saragadam *et al.*, "WIRE: Wavelet implicit neural representations" in *2023 IEEE/CVF Conference on Computer Vision and Pattern Recognition* (IEEE, Vancouver, Canada, 2023), pp. 18507–18516.
50. V. Sitzmann *et al*., "Implicit neural representations with periodic activation functions" in *34th Conference on Neural Information Processing Systems* (IEEE, Vancouver, Canada, 2020), pp. 7462–7473.
51. H. Pan, T. Blu, P. L. Dragotti, Sampling curves with finite rate of innovation. *IEEE Trans. Signal Process.* **62**, 458–471 (2014).
52. G. Tortarolo, M. Castello, A. Diaspro, S. Koho, G. Vicidomini, Evaluating image resolution in stimulated emission depletion microscopy. *Optica* **5**, 32–35 (2018).
53. J. Li *et al*., Code from "Nanoscale chemical imaging with structured X-ray illumination." GitHub. https://github.com/YijinLiu-Lab/NxSCI. Accessed 23 October 2023.